

## Article

# Ternary Hybrid Materials for Highly Sensitive Acetone Sensing at Room Temperature

Nurul Athirah Abu Hussein<sup>1,2,\*</sup>, Yew Hoong Wong<sup>3</sup>, Zainal Arif Burhanudin<sup>1,2</sup>  
and Huzein Fahmi Hawari<sup>1,2,\*</sup>

<sup>1</sup> Department of Electrical and Electronic Engineering, Universiti Teknologi Petronas, Seri Iskandar 32610, Malaysia; zainalarif.burhanudin@utp.edu.my

<sup>2</sup> Centre of Innovative Nanostructure and Nanodevices (COINN), Universiti Teknologi Petronas, Seri Iskandar 32610, Malaysia

<sup>3</sup> Centre of Advanced Materials, Department of Mechanical Engineering, Faculty of Engineering, Universiti Malaya, Kuala Lumpur 50603, Malaysia; yhwong@um.edu.my

\* Correspondence: nurulathirah.naah@gmail.com (N.A.A.H.); huzeinfahmi.hawari@utp.edu.my (H.F.H.)

**Abstract:** The performance of a conventional metal oxide sensor (MOX) is highly dependent on its high operating temperature. Many researchers have tried to solve the problem by exploring hybrid materials. On the other hand, ternary hybrid materials have emerged as a promising class of materials with unique properties and potential applications in various fields, be it environmental or medical, such as in breath analyzers for prediabetes analysis. This article focuses on the synthesis method, characterization, and application of ternary hybrid materials for room-temperature sensors, as well as recent advances and future developments in the field. The materials consist of three different components, metal oxide (Fe<sub>3</sub>O<sub>4</sub>), polymer (polyaniline) and carbon-based materials (reduced graphene oxide), which were synthesized using in-situ methods. Five samples were prepared in different ratios. The properties of these materials were characterized using techniques such as X-ray diffraction (XRD), Raman, scanning electron microscope (SEM) and transmission electron microscopy (TEM). The XRD and Raman analyses showed the existence of all the individual constituents in the hybrid sample. SEM and TEM also showed a strong interaction between the constituent materials as a hybrid nanocomposite. The response and recovery time were studied against 1, 10 and 100 ppm acetone. The results show that the sample with 10 wt%Fe<sub>3</sub>O<sub>4</sub>-PANI-RGO (S2\_10) has a reaction and recovery time < 32 s against the above ppm and has the highest sensing response at room temperature.

**Keywords:** ternary hybrid materials; room temperature; VOC sensing; acetone



**Citation:** Abu Hussein, N.A.; Wong, Y.H.; Burhanudin, Z.A.; Hawari, H.F. Ternary Hybrid Materials for Highly Sensitive Acetone Sensing at Room Temperature. *Crystals* **2023**, *13*, 845. <https://doi.org/10.3390/cryst13050845>

Academic Editors: Radu Claudiu Fierascu and Florentina Monica Raduly

Received: 18 April 2023

Revised: 11 May 2023

Accepted: 16 May 2023

Published: 20 May 2023



**Copyright:** © 2023 by the authors. Licensee MDPI, Basel, Switzerland. This article is an open access article distributed under the terms and conditions of the Creative Commons Attribution (CC BY) license (<https://creativecommons.org/licenses/by/4.0/>).

## 1. Introduction

### 1.1. Background

Breath is the largest potential source of volatile organic compounds (VOCs) and is also an important indicator of invasive or non-invasive medical diagnosis and health surveillance [1,2]. More than 870 types of volatile organic compounds (VOCs) can be detected in human breath. These VOCs provide important information about metabolic abnormalities or malfunctions in the human body [2], such as cancer [3], cystic fibrosis [4] and diabetes [5,6]. Diabetes is a common health problem in which patients have high blood glucose levels because the body is unable to produce sufficient amounts of insulin [5,7]. Despite enormous efforts to prolong the lives of diabetics, diabetes remains the fifth leading cause of death worldwide with 1.6 million deaths [5]. For early detection of diabetics, acetone gas concentration can be used as a marker to distinguish diabetics from healthy individuals. The acetone concentration in exhaled air is reported to be usually between 0.2 and 0.8 ppm in healthy people, while the threshold for diabetics is 1.8 ppm [8].

In general, gas sensors based on metal oxides are the most promising for monitoring harmful volatile organic compounds (VOCs). They are in great demand in many fields,

such as climate, safety, security, and process monitoring as well as for medical devices such as respiratory gas analyzers for the pre-diagnosis of diabetes. However, due to their high operating temperature of up to over 150 °C, the performance of the sensors degrades over time [7,9]. The discovery of hybrid materials generated a lot of interest in various fields. These are basically materials that consist of two or more different components and can combine the advantageous properties of each component to create new or improved functionalities [10]. Over the years, the applications of hybrid materials have expanded to many fields, such as medicine [11], batteries [12], supercapacitors [13], energy storage [14,15] and sensing [16–19].

In the field of sensor technology, a good sensor should be inexpensive, reliable, stable and easy to manufacture. Hybrid materials can improve the sensitivity, selectivity, stability, and reproducibility of a sensor [20,21]. Hybridization between materials is considered a promising strategy to overcome the drawbacks of organic and inorganic materials for gas sensing. It offers new or enhanced functionalities through a synergic interaction between the two phases [22–24]. So far, different materials, such as inorganic semiconductors, metal oxides and conducting polymers, have been used to fabricate sensors with a small size, low power consumption, high sensitivity, and high reliability [16,22,25–27].

By taking advantage of the hybridizing materials, the performance of the sensor can be improved. Some of the materials that can be used for hybridization with metal oxides are derivatives of graphene that is reduced to graphene oxide (RGO) and polymers such as polyaniline. The functional groups in RGO have been found to interact strongly with various gases, making RGO a promising platform for room-temperature chemical gas sensing applications [28]. On the other hand, the combination of polymers with iron oxide nanoparticles has attracted much attention in conductive polymer applications due to their structures as well as their chemical and physical properties. It has been proven that the hybridization of iron oxide on the network of the polymer material results in better conductivity and magnetization by generating an electromagnetic field (EM) [17,29,30]. Many researches have been carried out and have shown the advantages of inorganic compounds in the PANI matrix, especially magnetite ( $\text{Fe}_3\text{O}_4$ ).  $\text{Fe}_3\text{O}_4$  has good ferromagnetic properties and is resistant to corrosion by acidic solutions. Since  $\text{Fe}_3\text{O}_4$  is a hydrophobic material, chemical reactions with PANI increase its dispersions in solution. It also shows good electrical behavior when an external electric field is applied to the material [29].

### 1.2. Sensing Mechanism

The metal oxide gas sensor works on the principle of chemoresistance, where the gas molecules interacting with the metal oxides act either as donors or acceptors of charge carriers and change the resistance of the metal oxide. The increase or decrease in the resistance of the metal oxide thin film depends on the type of majority carriers in the semiconductor layer and the type of gas molecules (oxidizing or reducing) in the surrounding atmosphere. For n-type materials, oxidizing gases (acceptor) increase the resistance of the thin film, while reducing gases (donor) decrease the resistance, and vice versa for p-type materials [7]. When the sensor is exposed to the atmosphere, oxygen is adsorbed on the surface of the metal oxide and oxidation of the oxygen molecules takes place, with the oxygen atom accepting excited electrons from the conduction band of the metal oxide and becoming oxygen ions ( $\text{O}_2^-$ ,  $\text{O}^-$ ,  $\text{O}^{2-}$ ), and the reaction equations are (1)–(4) [31]. The resistance of the sensor remains the same if the ambient factor remains unchanged.



In the present work, we propose the preparation of a novel active material from the ternary hybrid material  $\text{Fe}_3\text{O}_4$ -PANI-RGO for the detection of acetone at room temperature. To the best of our knowledge, there are papers mentioning the hybridization of the proposed materials but none addressing the application for pre-diabetes diagnosis.

## 2. Materials and Methods

### 2.1. Materials

Iron (II) Chloride Tetrahydrate ( $\text{FeCl}_2 \cdot 4\text{H}_2\text{O}$ ), Iron (III) Chloride Hexahydrate ( $\text{FeCl}_3 \cdot 6\text{H}_2\text{O}$ ), Iron (III) Nitrate ( $\text{Fe}(\text{NO}_3)_3 \cdot 9\text{H}_2\text{O}$ ), Ammonium hydroxide (25%), Nitric acid (65%), Hydrochloric acid (37%), Aniline (99%), Ammonium peroxydisulfate (98%) Silver (Ag) paste (resistivity 30–35  $\mu\Omega\text{-cm}$ ), Ascorbic Acid and Graphene oxide (GO) paste (95 wt% purity) were all purchased from Merck. De-ionized (DI) water was used in all preparations. Interdigitated electrode (IDE) with a size of 5 mm  $\times$  5 mm was purchased from Nova Scientific (Sturbridge, MA, USA).

### 2.2. Synthesis of Ternary Hybrid Nanocomposite $\text{Fe}_3\text{O}_4$ -PANI-RGO

The ternary hybrid nanocomposite was prepared by an in-situ method, as shown in Figure 1, where the as-synthesized  $\text{Fe}_3\text{O}_4$  and PANI were first sonicated in a bath for 30 min. Then both solvents were added and mixed with the GO paste for another 1 h to ensure homogeneity. Then, 0.1 g ascorbic acid was added to the mixture and heated to 90 °C for 2 h. Finally, the product was centrifuged and washed with ethanol and water. The dry product was obtained by drying the mixture in an oven. The synthesis process is illustrated in Figure 1. Five different samples were synthesized with different weight ratios of the materials. The name and description of the samples are listed in Table 1.

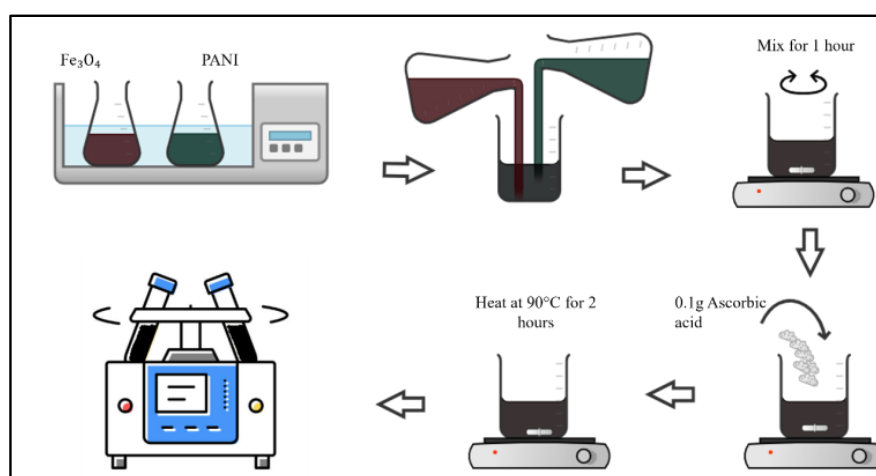


**Figure 1.** Synthesis process of ternary hybrid materials.

**Table 1.** Sample name and description of the ratios used.

Sample Name	Description
S1_5	5 wt% $\text{Fe}_3\text{O}_4$ -PANI-90 wt%RGO
S2_10	10 wt% $\text{Fe}_3\text{O}_4$ -PANI-80 wt%RGO
S3_20	20 wt% $\text{Fe}_3\text{O}_4$ -PANI-60 wt%RGO
S4_30	30 wt% $\text{Fe}_3\text{O}_4$ -PANI-40 wt%RGO
S5_40	40 wt% $\text{Fe}_3\text{O}_4$ -PANI-20 wt%RGO

### 2.3. Thin-Film Development and Gas-Sensing Setup

Figure 2 shows the diagram of the development of the thin film on IDE and the construction of the gas sensor. A volume 1.0  $\mu\text{L}$  was developed on the IDE using the drop casting method. The thin film was then dried at room temperature. For the measurement setup, the IDE chamber was connected to the outlet tube of the air and VOC and the multimeter.

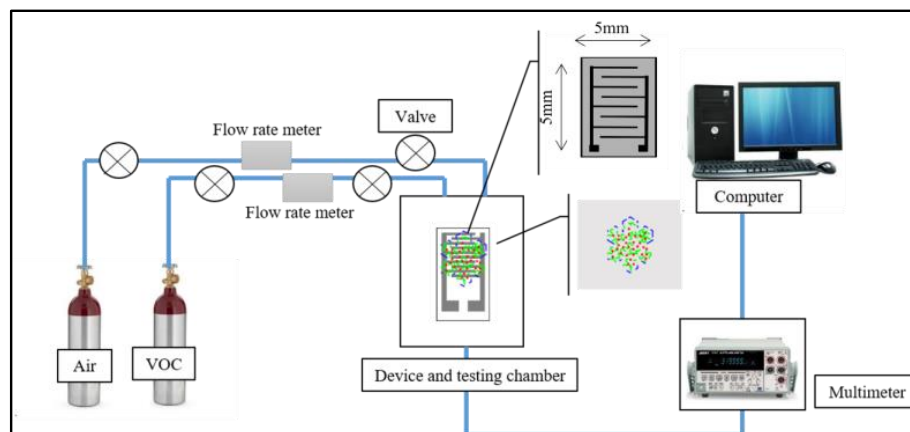


**Figure 2.** Gas-sensing setup.

### 2.4. Characterization

Microstructural analysis of the synthesized active materials was studied using an x-ray diffractometer (XRD) (Panalytical, model X'Pert<sup>3</sup> Powder, Malvern, UK), structural and morphological analysis was performed using Raman spectroscopy (Horiba, model HR800, 514 nm laser excitation, Kyoto, Japan) for the spectral ranges of 200 to 4000  $\text{cm}^{-1}$ , scanning electron microscope (SEM) (Tescan Vega, Brno, Czech Republic) and transmission electron microscope (TEM) (Hitachi, model HT7830, Tokyo, Japan).

A specially designed vapor sensor setup was used to investigate the performance of the active materials at room temperature. The IDE was placed in a chamber and connected to the multimeter. First, air was purged onto the  $\text{Fe}_3\text{O}_4$ -PANI-RGO-coated IDE for 60 s, then, VOC (acetone) was purged onto the IDE. The analyte from the vapor was adsorbed on the surface of the active materials, resulting in changes in the impedance and capacitance of the IDE due to the polarization and realignment of molecules in the dielectric materials. The process was continued with the purging of air to desorb the analyte from the surface of the active materials. The response and recovery time were monitored in real time on the connected computer.

## 3. Results and Discussion

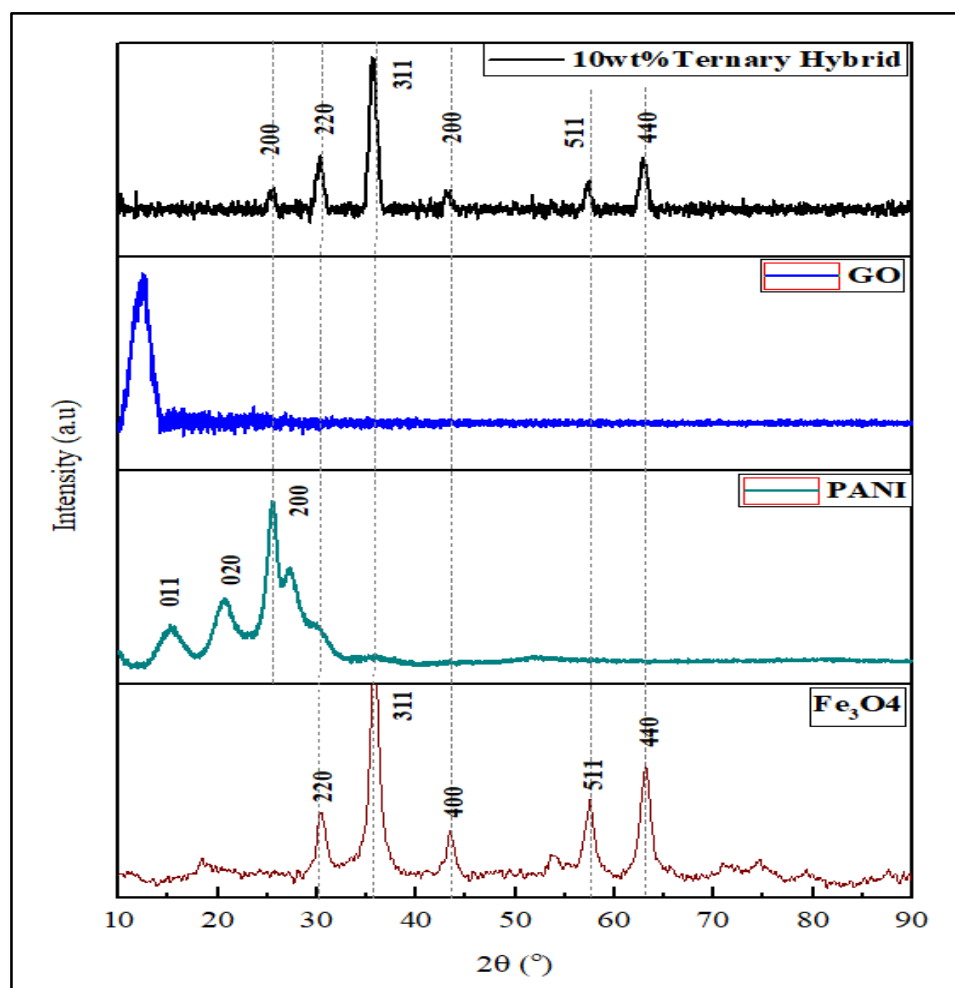
### 3.1. Microstructural Analysis

The microstructural analysis of the materials was investigated by XRD. The pattern consists of the as-synthesized  $\text{Fe}_3\text{O}_4$ , PANI, GO and S2\_10 and is shown in Figure 3. For PANI, the peaks are found to be at  $2\theta$ : 15.1, 20.7, 25.5 and 27.3° with corresponding d-spacings of 5.9, 4.3, 3.5, and 3.3 Å, which are very similar to those in the study conducted by (Singu et al., 2011) [32]. For graphene oxide (GO), the main peak is at about  $\sim 12.5^\circ$ , indicating the presence of amorphous GO. The disappearance of this peak in sample S2\_10 indicates the complete reduction GO to RGO [33]. The integration of the plane with  $\text{Fe}_3\text{O}_4$  and PANI reveals the low crystallinity of RGO and shows a large interfacial contact between all the constituent materials [34,35]. For  $\text{Fe}_3\text{O}_4$ , all peaks showed consistent agreement with ICDD Card No. 98-015-8746, where the strong and sharp diffraction peaks were seen at  $2\theta$ : 30.3, 35.7, 43.2, 53.8, 57.3 and 62.9°, corresponding to the  $d_{200}$ ,  $d_{311}$ ,  $d_{400}$ ,  $d_{422}$ ,  $d_{511}$  and  $d_{440}$  planes respectively. The calculated cubic lattice parameter was 8.33 Å,

which is in agreement with the findings reported in the literature review [35]. The crystallite size of the samples was calculated using the Debye–Scherrer equation:

$$D = \frac{k\lambda}{\beta \cos\theta} \quad (5)$$

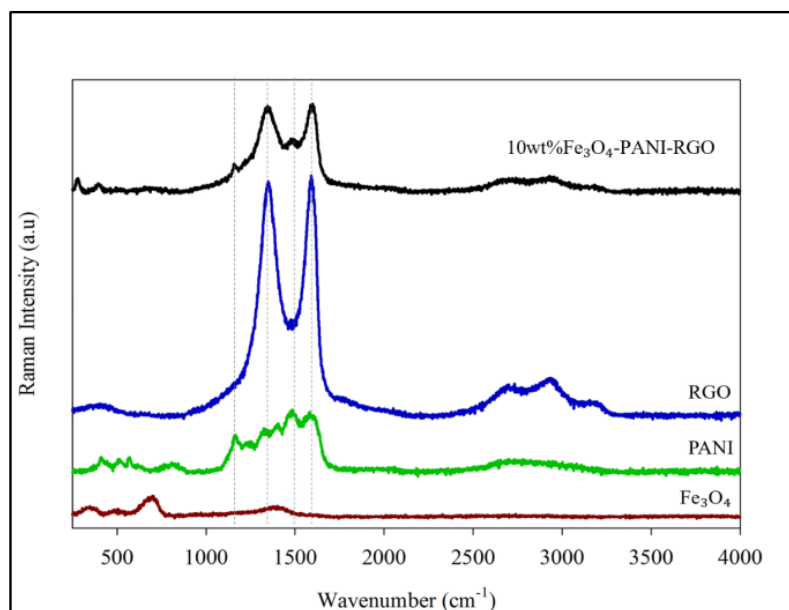
where  $D$  is the particle size (nm),  $k$  is a constant ( $k = 0.94$ ),  $\lambda$  is the x-ray wavelength,  $\beta$  is the full width at half maximum (FWHM) of the diffraction peak, and  $\theta$  is the angle of diffraction. The crystallite size calculated from (Equation (5)) for the samples  $\text{Fe}_3\text{O}_4$ , PANI and S2\_10 were  $9.68 \pm 1.9$ ,  $4.17 \pm 3.2$  and  $9.34 \pm 1.4$  nm, respectively.



**Figure 3.** XRD analysis of  $\text{Fe}_3\text{O}_4$ , PANI and S2\_10.

### 3.2. Raman Analysis

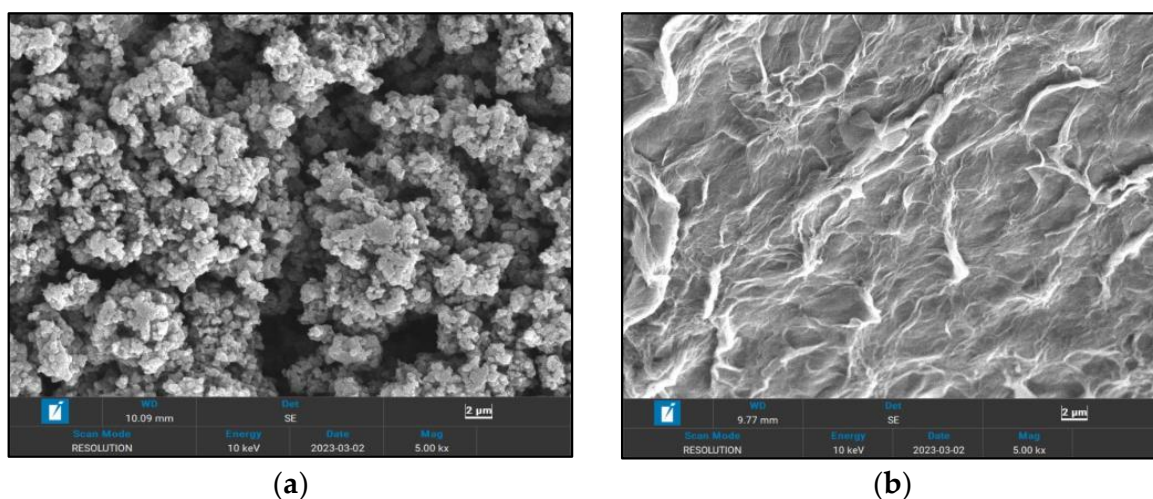
Raman spectroscopic analysis was performed to verify the presence of PANI and RGO. Figure 4 shows two observation peaks at  $1345 \text{ cm}^{-1}$  and  $1594 \text{ cm}^{-1}$  for the ternary hybrid material sample, indicating the D and G bands of GO. While the G band correlates to the  $\text{sp}^2$ -hybridized graphitic carbon atoms in RGO, the D band is related to structural defects and disorder of RGO [36,37]. When comparing the single constituents of RGO with sample S1\_10, it was found that the  $I_D/I_G$  decreased from 0.975 to 0.969, which is related to the reduction of the defect following the PANI coating [38]. Two other small peaks from sample S1\_10 can be seen at  $1157$  and  $1484 \text{ cm}^{-1}$ , which represent the C-H vibration in the quinoid and semiquinone structures of PANI and show the establishment of a PANI chain on GO for the ternary hybrid nanocomposite material [39].



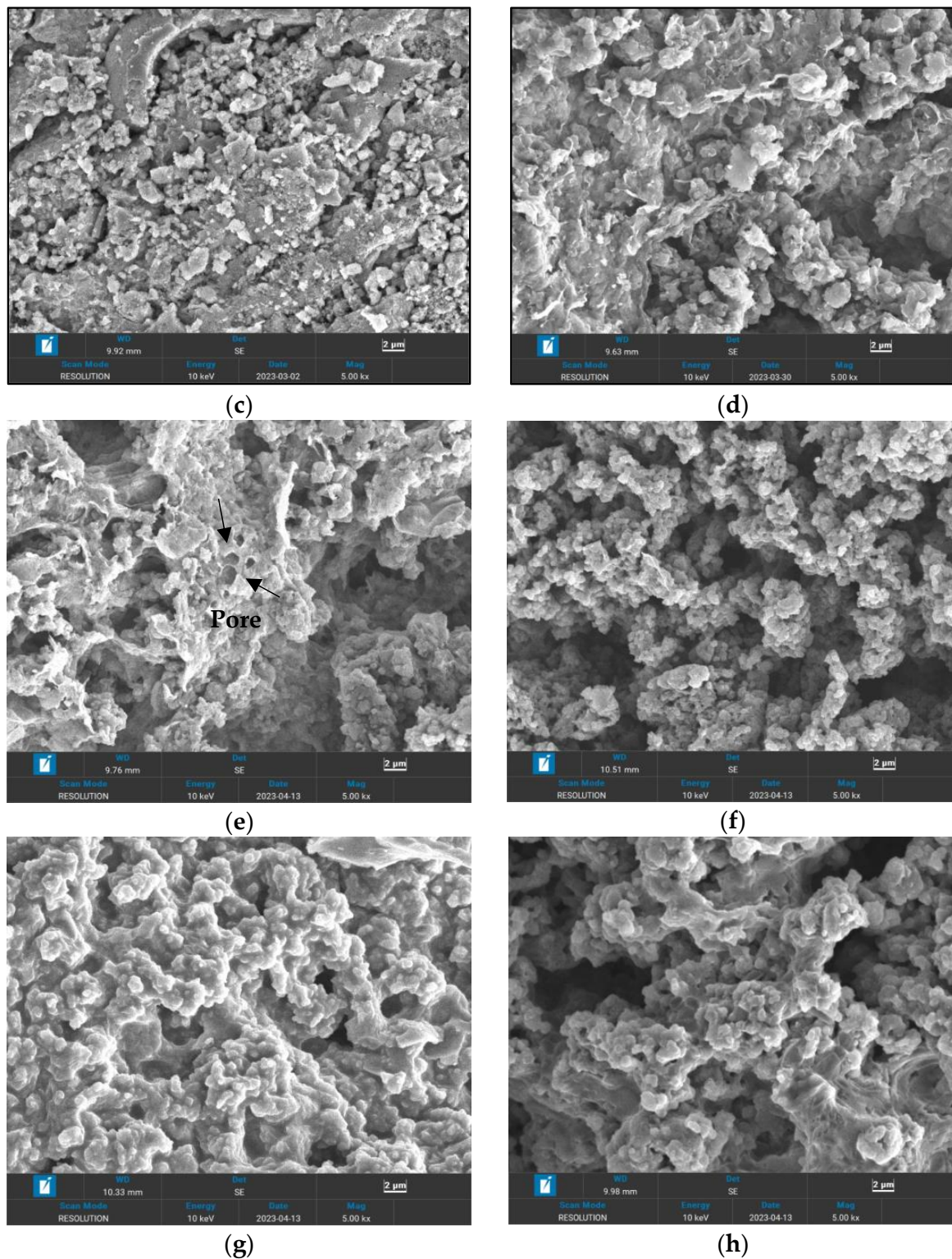
**Figure 4.** Raman analysis of the single constituents and the ternary hybrid nanocomposite material of sample S2\_10.

### 3.3. Morphological Analysis

The structure and morphology of the as-synthesized individual components of Fe<sub>3</sub>O<sub>4</sub>, PANI and RGO as well as the ternary hybrid material were investigated by SEM and TEM analysis. Figure 5a shows the SEM image of RGO, where a clear, wrinkled surface at a magnification of 2  $\mu\text{m}$  can be seen. Figure 5b,c show the image of PANI with a high porosity and a rough crystalline image of Fe<sub>3</sub>O<sub>4</sub>, respectively. The agglomeration of Fe<sub>3</sub>O<sub>4</sub> is due to its highly magnetic properties [38]. The porosity of PANI could be useful for the absorption of analyte during the sensing process, as it will provide a more active site [40,41]. Figure 5d–h show the ternary hybrid nanocomposite samples of S1\_5, S2\_10, S3\_20, S4\_30 and S5\_40, showing a similar morphology to the single constituent materials, with hole-like porosity evident for all concentrations of the hybrid materials. A dense PANI and Fe<sub>3</sub>O<sub>4</sub> nanomaterial is seen coated on the sheet-like RGO. This proves that PANI and Fe<sub>3</sub>O<sub>4</sub> are evenly distributed on the surface of RGO.



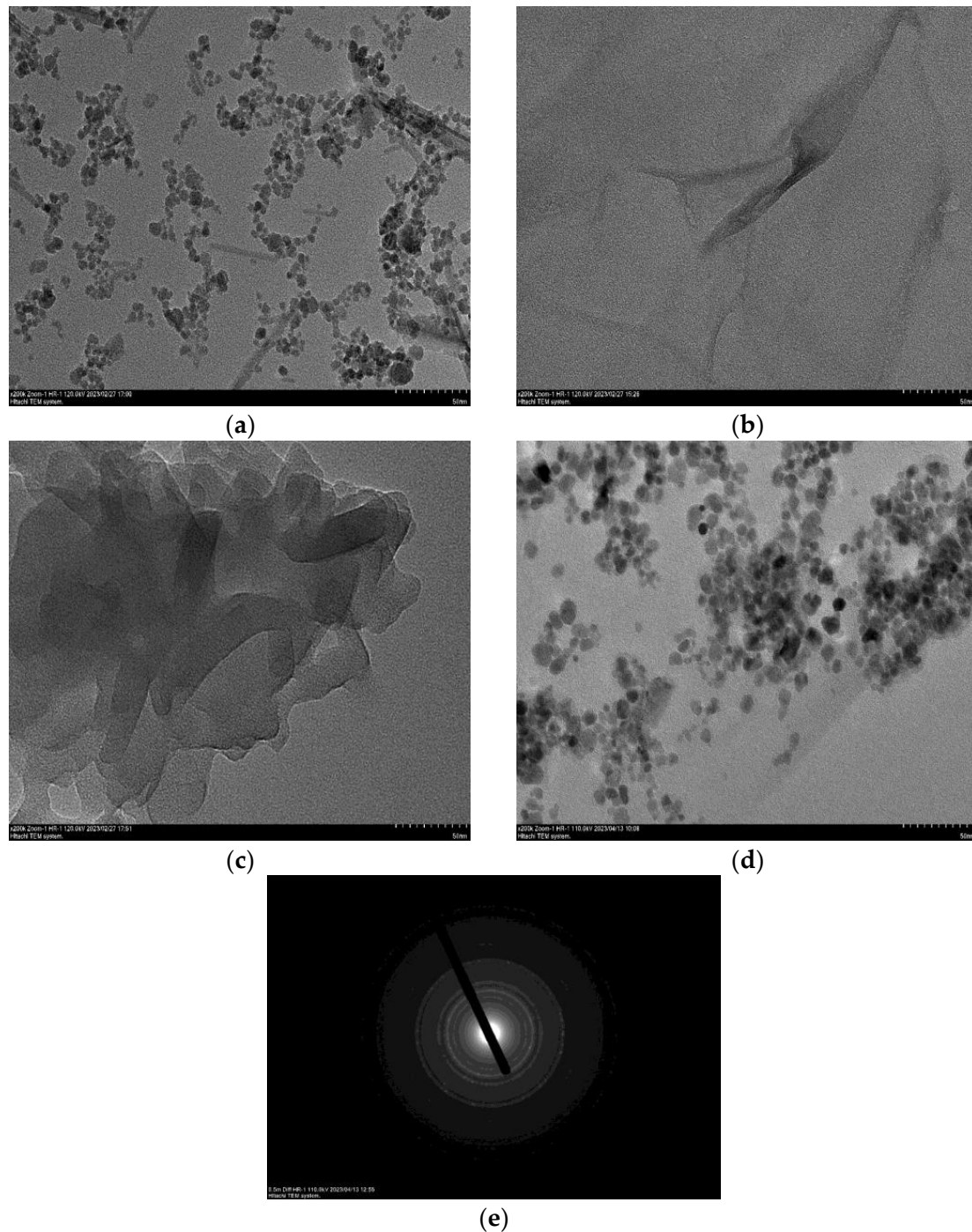
**Figure 5.** Cont.



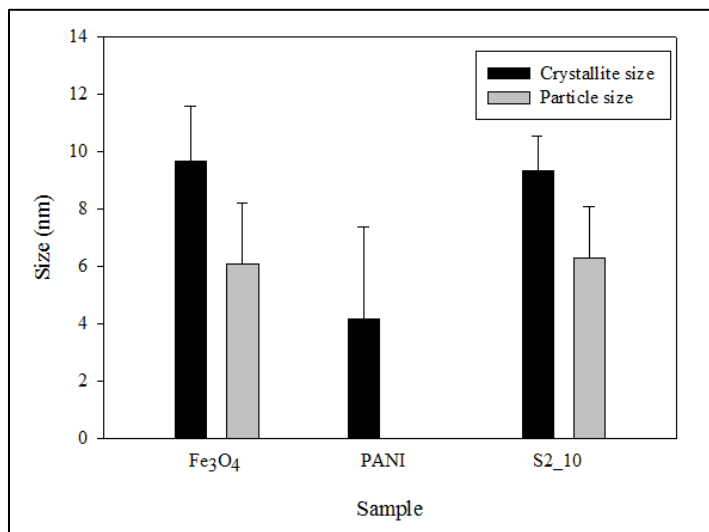
**Figure 5.** SEM Images of (a) RGO, (b) PANI, (c) Fe<sub>3</sub>O<sub>4</sub> and (d–h) S1\_5, S2\_10, S3\_20, S4\_30 and S5\_40, respectively.

TEM analyses of the single material Fe<sub>3</sub>O<sub>4</sub>, RGO, PANI, the ternary hybrid sample S2\_10 and the SAED diffraction are shown in Figure 6a–e, respectively. The single-material Fe<sub>3</sub>O<sub>4</sub> shows a spherical shape with different sizes and a low aggregation with an average particle size of  $6.1 \pm 2.1$  nm, which complements the crystallite size from XRD, as shown in Figure 7. RGO shows a common sheet-like structure with a smooth surface, which is con-

sistent with the image from SEM. This result is similar to the study reported by Gupta et al. (2022) [42]. PANI shows a rod-like structure due to the electrostatic interaction [41]. The size of the rod-like structure is about 15–23 nm in diameter. Figure 6d shows sample S2\_10, which has a similar structure to  $\text{Fe}_3\text{O}_4$ , with the spherical shape of  $\text{Fe}_3\text{O}_4$  incorporated with PANI uniformly located on the surface of the RGO sheet. The calculated particle size was  $6.3 \pm 1.8$  nm. These findings support the synthesis of the ternary hybrid nanocomposite with an excellent dispersion. Figure 6e shows the selected area diffraction pattern (SAED) of sample S2\_10, in which a well-defined diffraction ring can be seen in agreement with planes (200), (220), (311), (400), (422), (511) and (440), complementing the XRD result.



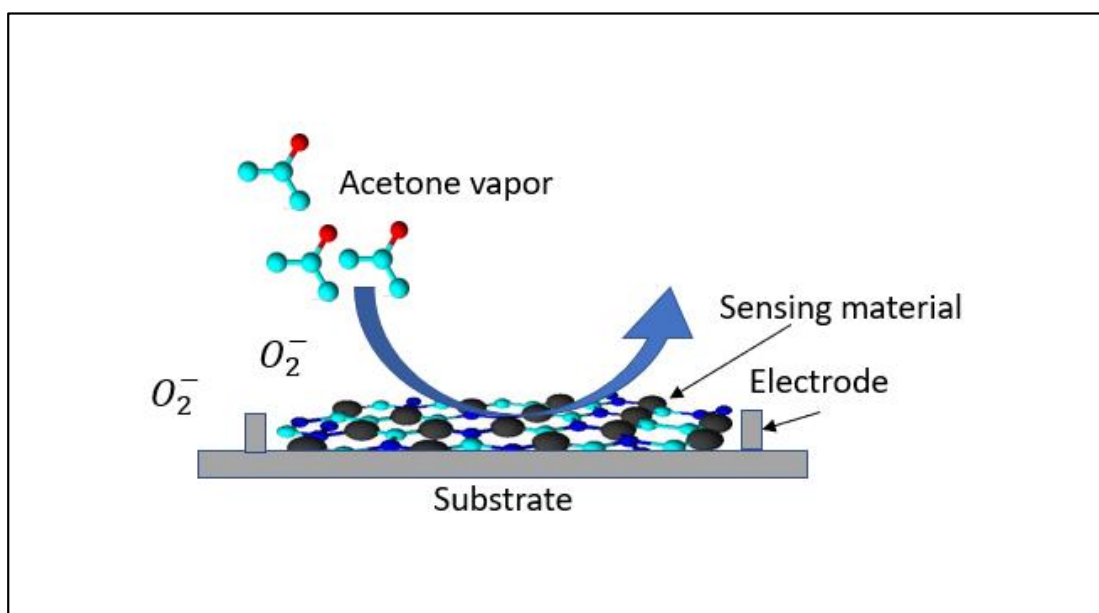
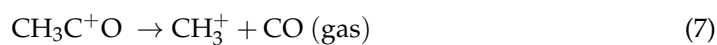
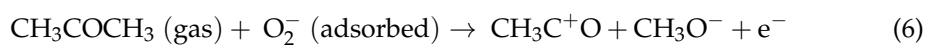
**Figure 6.** TEM analysis for samples (a)  $\text{Fe}_3\text{O}_4$ , (b) RGO, (c) PANI and (d) S2\_10, and (e) SAED pattern.



**Figure 7.** Crystallite size and particle comparison from XRD and TEM respectively.

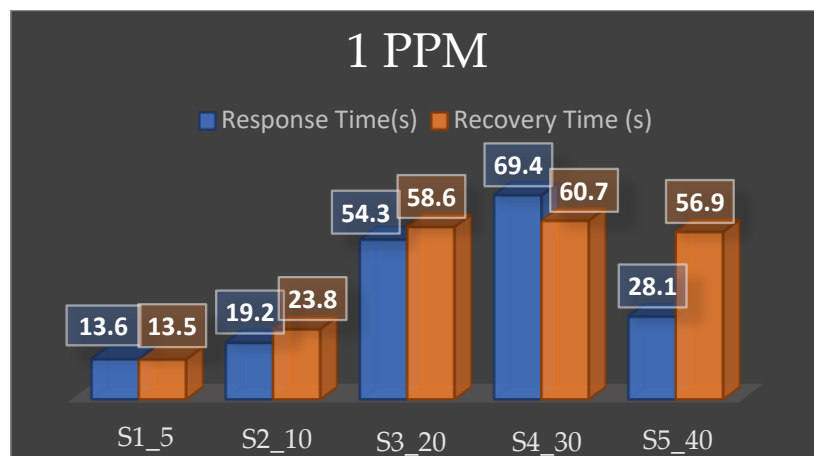
### 3.4. Sensing Analysis

Figure 8 shows the schematic diagram of the sensor mechanism. When the metal oxide sensor is placed in an environment with the presence of target gas, the target gas will react with the oxygen species on the surface of the active material (Equations (1)–(4)). The interaction between the target gas and the oxygen species will create a resistance change in the sensor. For acetone, the reaction is simplified as follows [43]:

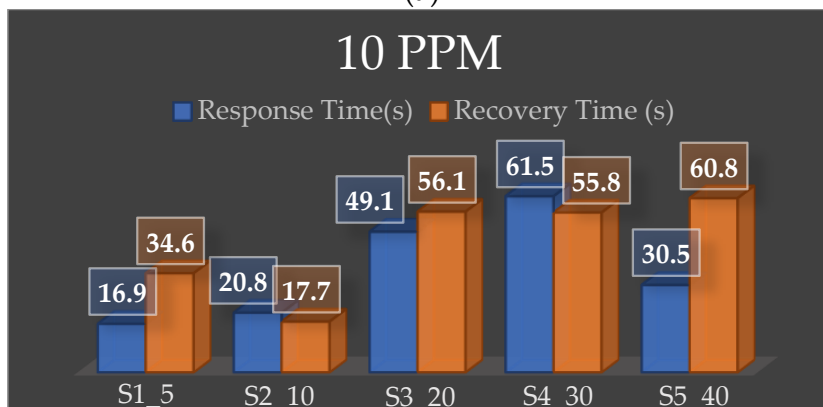


**Figure 8.** The mechanism of the sensor towards acetone vapor.

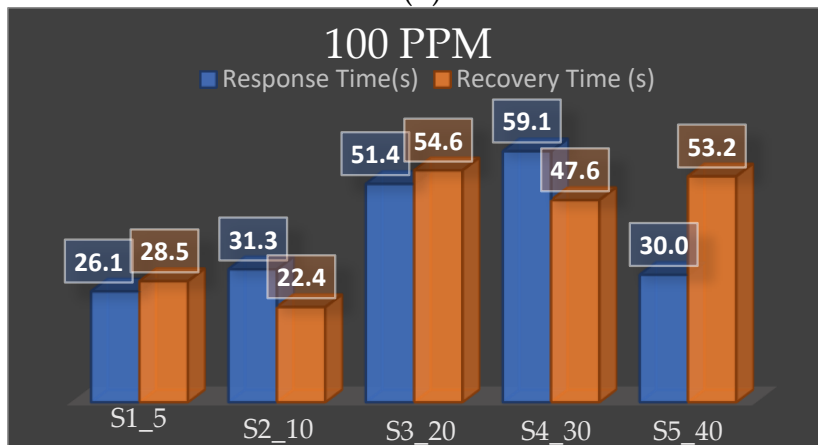
Figure 9a–c show the response and recovery time for all samples when expose to 1, 10, and 100 ppm acetone, respectively, while Figure 10a–c show the real-time response of samples S2\_10 when expose to 1, 10, and 100 ppm acetone, respectively. The response time is defined as the time from the first contact of the sensor with acetone vapor, in which the sensor resistance reaches 90% of the saturated value of the resistance to acetone vapor. The recovery time is the time from which the acetone resistance returns to 10% of the baseline [44]. To imitate the most common environment for the gas sensor, air was used as the carrier gas.



(a)

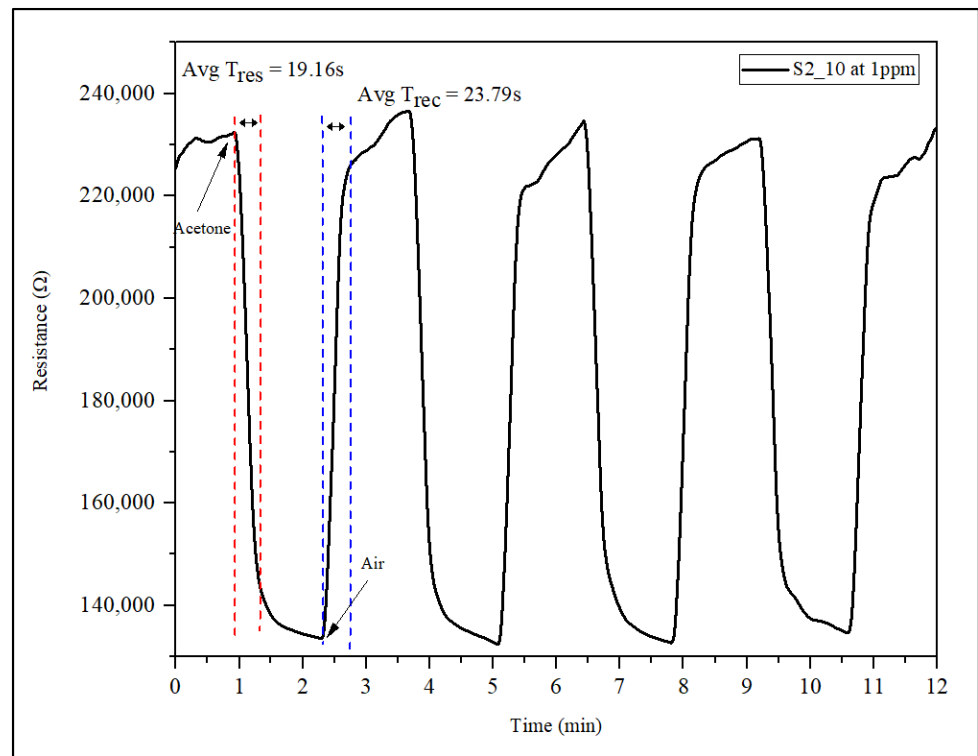


(b)

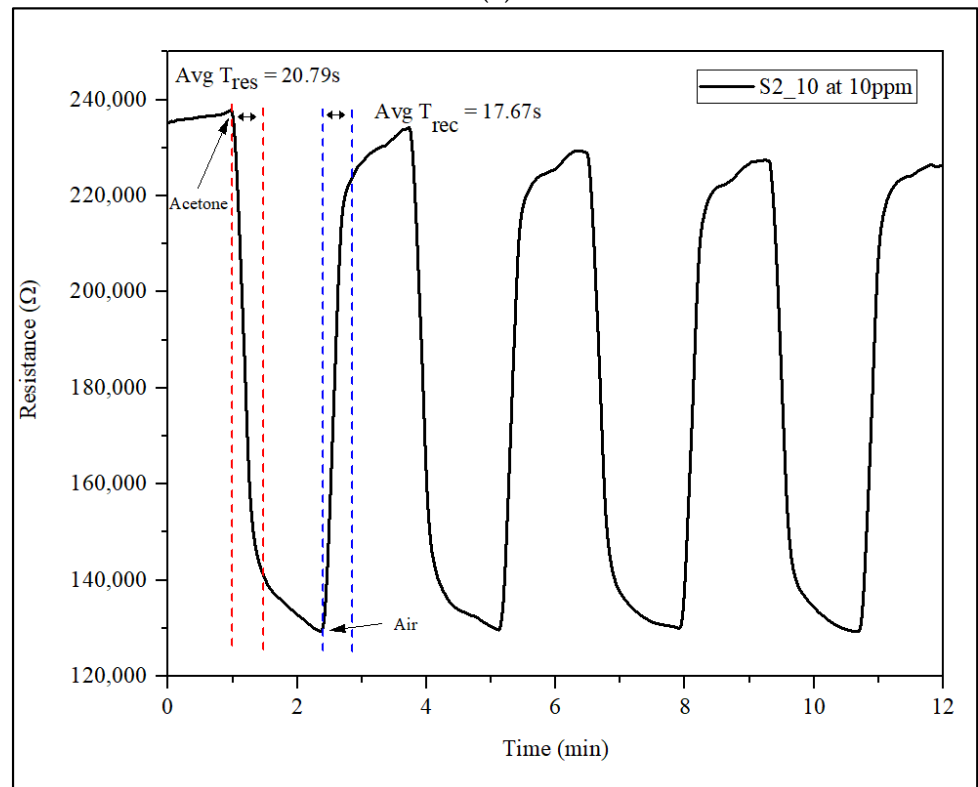


(c)

**Figure 9.** The response and recovery time in seconds for all samples to (a) 1, (b) 10 and (c) 100 ppm acetone vapor.

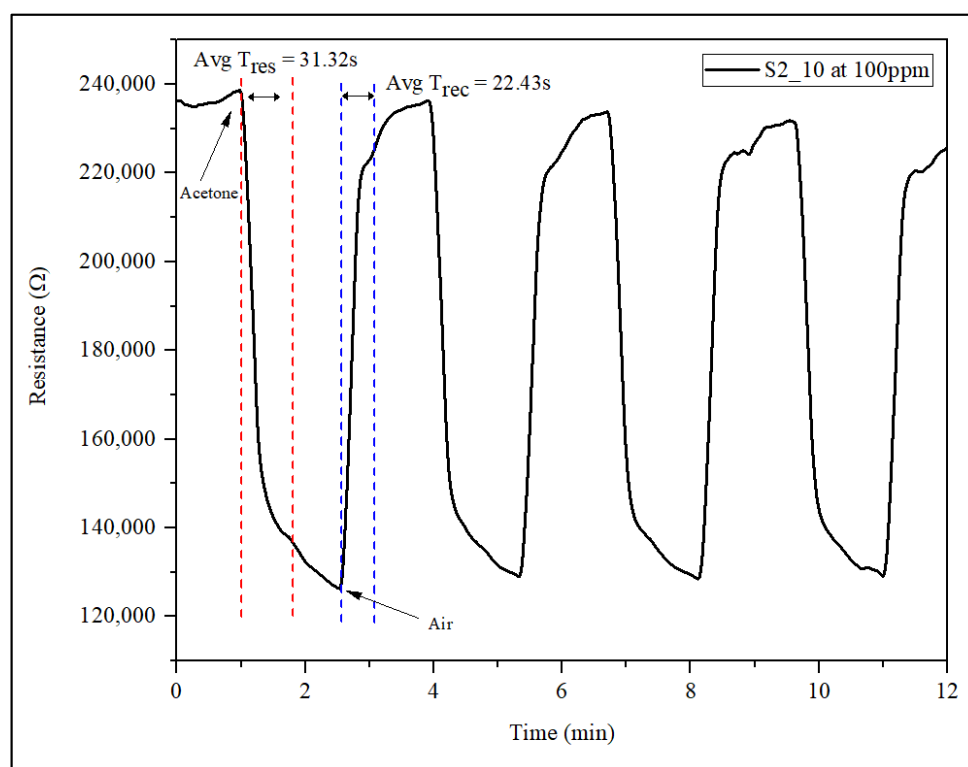


(a)



(b)

Figure 10. Cont.



(c)

**Figure 10.** The response of IDE sensor of all samples to (a) 1, (b) 10 and (c) 100 ppm acetone, respectively.

From the response in Figure 10, we can see that the resistance of the samples decreases/increases upon exposure to acetone and gradually stabilizes. The response shows a concentration-dependent behavior depending on the charge carrier [45]. When p-type semiconductors meet n-type semiconductors, the holes in the p-type semiconductors diffuse into the n-type semiconductors and neutralize the free electrons, resulting in the generation of synergistic positive charges in the n-type semiconductors. This explains the emergence of a synergistic effect between the organic p-type material (PANI) and the n-type material (RGO-Fe<sub>3</sub>O<sub>4</sub>) [45,46]. From our previous work, the response and recovery time of Fe<sub>3</sub>O<sub>4</sub> to 300 ppm acetone at 300 °C was 2.19/3.6 min, respectively [47]. Based on the current work, the response and recovery time are of which is shown in Figure 9, sample S1\_5 had the fastest response and recovery time to 1 ppm acetone, which was 13.6 s/13.5 s, respectively. When exposed to 10 and 100 ppm acetone, sample S2\_10 had a better response and recovery time compared to the other samples, with measurements of 20.8 s/17.7 s and 31.3 s/22.4 s, respectively. The performance of the sensor improves at a lower ppm of acetone and at the lower operating temperature, i.e., room temperature. This could be due to an increase in the size of the analyte site leading to an increase in the detected signal as well as the sensitivity of the sensor. One of the reasons for the increasing sensitivity is the pore that can be seen in the SEM image [48]. It was reported by Abokifa et al. (2019) that the sensing at room temperature was attributed to some factors, such as the morphology, small grain size and high surface-to-volume ratio of the nanostructured sensors, as the above-mentioned mechanism (Equation (3)) only takes place under high-operating-temperature conditions (<200 °C) [31]. In this case, 10 wt% was the optimal ratio of the ternary hybrid, as increasing the ratio above this value resulted in the response and recovery time of the sensor also increasing. However, when the concentration was further increased to 40 wt%, the response/recovery time decreased. This finding proves that adjusting the active material

of the MOX sensor can affect the performance of the sensor, such as the sensitivity and the response and recovery times.

The sensing response of the sensor ( $S$ ) was calculated using the following equation:

$$S (\%) = \frac{(R_g - R_a)}{R_a} \times 100 \quad (9)$$

where  $R_g$  is the electrical resistance in the presence of gas, and  $R_a$  is the electrical resistance in the presence of air. The sensor response shown in Figure 11 for sample S2\_10 was observed for 42 days. It shows that the response does not vary significantly. This is due to some factors, such as the ability of the analyte molecules to be adsorbed on the surface of the active materials due to the pore volume [48]. This can be explained by the SEM image in Figure 5e, where the pore volume of sample S2\_10 can be obviously seen on the surface of the sample. Therefore, the improvement of the pore volume has a great influence on the sensitivity of the sample [49].

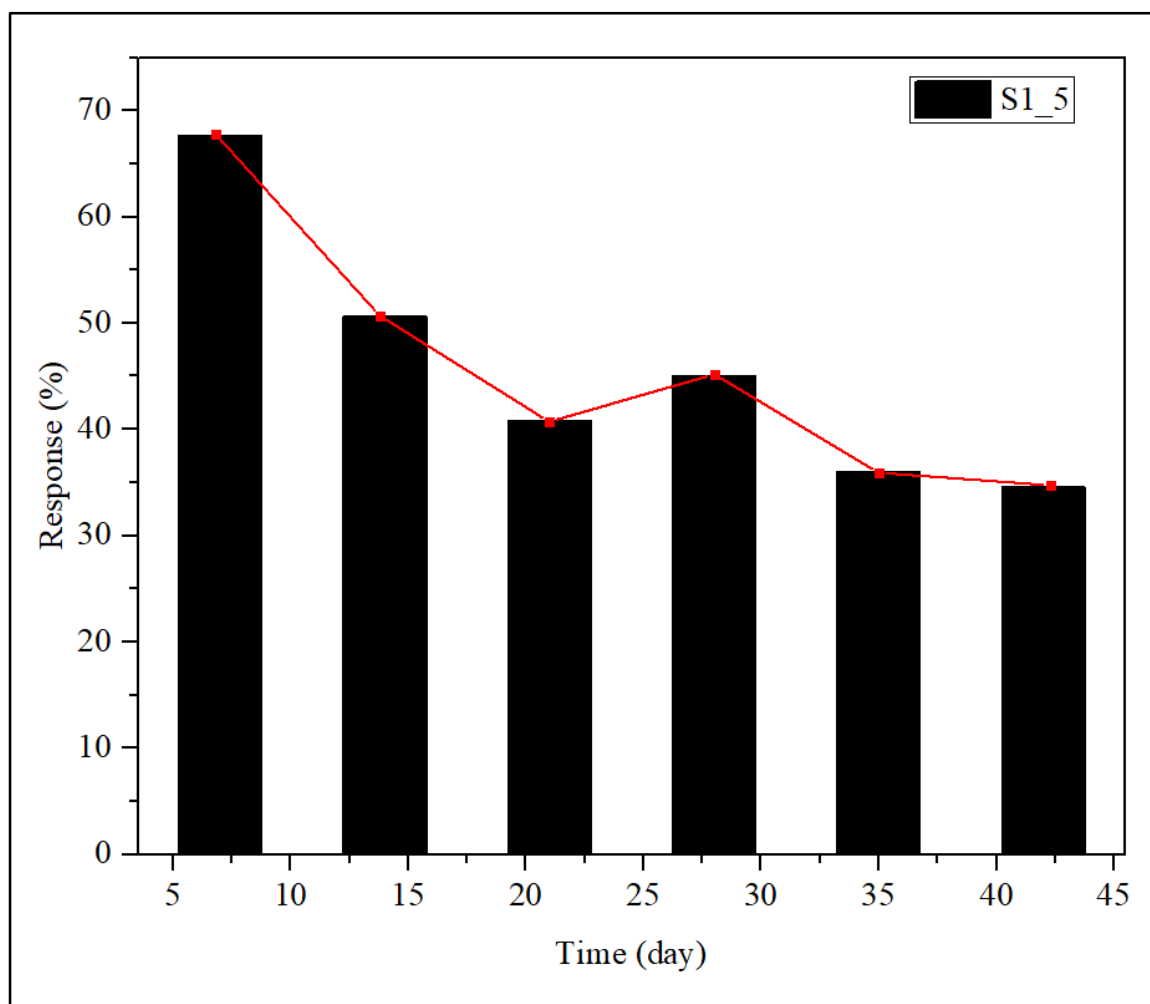


**Figure 11.** The stability of all samples to 1 ppm acetone at room temperature for seven weeks.

Figure 12 shows the sensory response of all samples when exposed to 1000 ppm formaldehyde, ethanol and acetone. It can be seen that sample S1\_5 reacts more strongly to formaldehyde, while samples S2\_10, S3\_20 and S4\_30 react three times more strongly to acetone compared to formaldehyde and ethanol. From this, we can conclude that sample S2\_10 has a high response to acetone and is suitable for breath analyzers for pre-diabetic diagnosis.

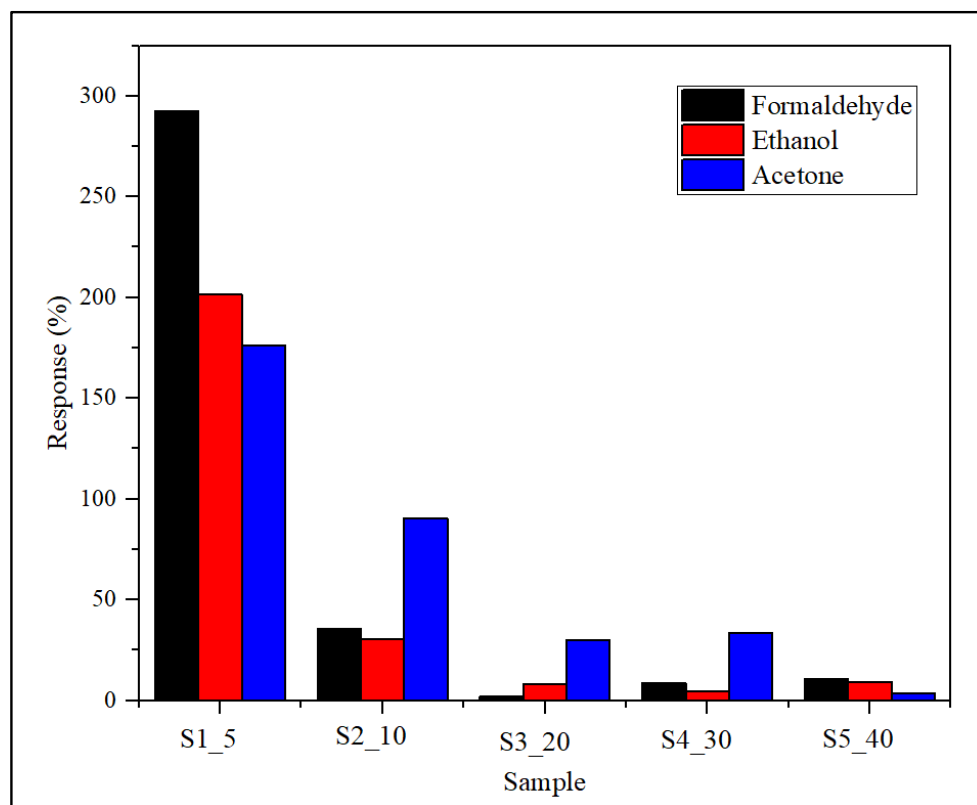


**Figure 12.** The selectivity response of the IDE sensor to 1000 ppm formaldehyde, ethanol and acetone at room temperature.

#### 4. Conclusions

In general, the ternary hybrid nanocomposite materials were synthesized and investigated for their sensing capability. The reaction and recovery time of the ternary hybrid material was studied for 1, 10 and 100 ppm acetone. The fastest response and recovery time for the lowest ppm of acetone was confirmed for sample S1\_5. However, as the concentration increased, the sensor response also increased. In this case, sample S2\_10 reacted the most to acetone vapor compared to the other samples. This could be due to several reasons, such as the depletion layer, the available active sites and the thickness of the samples cast on IDE. This shows that concentration is dependent on the performance of the sensor. However, further studies need to be carried out to investigate the chemical and physical properties of the active materials, so that modifications can be made to further reduce the reaction and recovery times and improve the sensitivity of the sensor.

**Author Contributions:** Conceptualization, N.A.A.H. and H.F.H.; Data curation, N.A.A.H.; Formal analysis, N.A.A.H.; Funding acquisition, H.F.H.; Investigation, N.A.A.H.; Methodology, N.A.A.H.; Project administration, H.F.H.; Resources, H.F.H.; Software, N.A.A.H.; Supervision, Y.H.W., Z.A.B. and H.F.H.; Validation, N.A.A.H.; Visualization, H.F.H.; Writing—original draft, N.A.A.H.; Writing—review & editing, N.A.A.H. and H.F.H. All authors have read and agreed to the published version of the manuscript.

**Funding:** This research was funded by the Ministry of Higher Education (MOHE) through the Fundamental Research Grant Scheme (Ref No. FRGS/1/2019/TK04/UTP/02/7).

**Data Availability Statement:** The data is available upon request from the corresponding author (N.A.A.H.).

**Acknowledgments:** The authors would like to thank Centralized Analytical Laboratory (CAL), UTP for their contributions in this publication.

**Conflicts of Interest:** The authors declare no conflict of interest.

## References

1. Zhang, D.; Hu, Y.; Chen, Y.; Zeng, B. BreathTrack: Tracking Indoor Human Breath Status via Commodity WiFi. *IEEE Internet Things J.* **2019**, *6*, 3899–3911. [\[CrossRef\]](#)
2. Zhou, X.; Xue, Z.; Chen, X.; Huang, C.; Bai, W.; Lu, Z.; Wang, T. Nanomaterial-based gas sensors used for breath diagnosis. *J. Mater. Chem. B* **2020**, *8*, 3231–3248. [\[CrossRef\]](#)
3. van Keulen, K.E.; Jansen, M.E.; Schrauwen, R.W.M.; Kolkman, J.J.; Siersema, P.D. Volatile organic compounds in breath can serve as a non-invasive diagnostic biomarker for the detection of advanced adenomas and colorectal cancer. *Aliment Pharm.* **2020**, *51*, 334–346. [\[CrossRef\]](#)
4. Woollam, M.; Siegel, A.P.; Grocki, P.; Saunders, J.L.; Sanders, D.B.; Agarwal, M.; Davis, M.D. Preliminary method for profiling volatile organic compounds in breath that correlate with pulmonary function and other clinical traits of subjects diagnosed with cystic fibrosis: A pilot study. *J. Breath Res.* **2022**, *16*, 027103. [\[CrossRef\]](#)
5. Khan, R.M.M.; Chua, Z.J.Y.; Tan, J.C.; Yang, Y.; Liao, Z.; Zhao, Y. From Pre-Diabetes to Diabetes: Diagnosis, Treatments and Translational Research. *Medicina* **2019**, *55*, 546. [\[CrossRef\]](#)
6. Dixit, K.; Fardindoost, S.; Ravishankara, A.; Tasnim, N.; Hoorfar, M. Exhaled Breath Analysis for Diabetes Diagnosis and Monitoring: Relevance, Challenges and Possibilities. *Biosensors* **2021**, *11*, 476. [\[CrossRef\]](#)
7. Zhang, H.; Xiao, J.; Wang, Y.; Zhang, L.; Zhao, G.; Yang, H.; Wang, H. A portable acetone detector based on SmFeO<sub>3</sub> can pre-diagnose diabetes through breath analysis. *J. Alloys Compd.* **2022**, *922*, 166160. [\[CrossRef\]](#)
8. Baharuddin, A.A.; Ang, B.C.; Haseeb, A.S.M.A.; Wong, Y.C.; Wong, Y.H. Advances in chemiresistive sensors for acetone gas detection. *Mater. Sci. Semicon Proc.* **2019**, *103*, 104616. [\[CrossRef\]](#)
9. Sharma, B.; Sharma, A.; Kim, J.-S. Recent advances on H<sub>2</sub> sensor technologies based on MOX and FET devices: A review. *Sens. Actuators B Chem.* **2018**, *262*, 758–770. [\[CrossRef\]](#)
10. Adnan, M.M.; Dalod, A.R.M.; Balci, M.H.; Glaum, J.; Einarsrud, M.A. In Situ Synthesis of Hybrid Inorganic(-)Polymer Nanocomposites. *Polymers* **2018**, *10*, 1129. [\[CrossRef\]](#) [\[PubMed\]](#)
11. Broza, Y.Y.; Har-Shai, L.; Jeries, R.; Cancilla, J.C.; Glass-Marmor, L.; Lejbkovicz, I.; Torrecilla, J.S.; Yao, X.; Feng, X.; Narita, A.; et al. Exhaled Breath Markers for Nonimaging and Noninvasive Measures for Detection of Multiple Sclerosis. *ACS Chem. Neurosci* **2017**, *8*, 2402–2413. [\[CrossRef\]](#)
12. Wu, S.; Fu, G.; Lv, W.; Wei, J.; Chen, W.; Yi, H.; Gu, M.; Bai, X.; Zhu, L.; Tan, C.; et al. A Single-Step Hydrothermal Route to 3D Hierarchical Cu<sub>2</sub>O/CuO/rGO Nanosheets as High-Performance Anode of Lithium-Ion Batteries. *Small* **2018**, *14*, 1702667. [\[CrossRef\]](#)
13. Lu, X.F.; Chen, X.Y.; Zhou, W.; Tong, Y.X.; Li, G.R. alpha-Fe<sub>2</sub>O<sub>3</sub>@PANI Core-Shell Nanowire Arrays as Negative Electrodes for Asymmetric Supercapacitors. *ACS Appl. Mater. Interfaces* **2015**, *7*, 14843–14850. [\[CrossRef\]](#) [\[PubMed\]](#)
14. Notarianni, M.; Liu, J.; Vernon, K.; Motta, N. Synthesis and applications of carbon nanomaterials for energy generation and storage. *Beilstein J Nanotechnol* **2016**, *7*, 149–196. [\[CrossRef\]](#)
15. Tabrizi, A.G.; Arsalani, N.; Naghshbandi, Z.; Ghadimi, L.S.; Mohammadi, A. Growth of polyaniline on rGO-CO<sub>3</sub>S<sub>4</sub> nanocomposite for high-performance supercapacitor energy storage. *Int. J. Hydrog. Energy* **2018**, *43*, 12200–12210. [\[CrossRef\]](#)
16. Ahmadi Tabr, F.; Salehiravesh, F.; Adelnia, H.; Gavgani, J.N.; Mahyari, M. High sensitivity ammonia detection using metal nanoparticles decorated on graphene macroporous frameworks/polyaniline hybrid. *Talanta* **2019**, *197*, 457–464. [\[CrossRef\]](#)
17. Bandgar, D.K.; Navale, S.T.; Mane, A.T.; Gupta, S.K.; Aswal, D.K.; Patil, V.B. Ammonia sensing properties of polyaniline/ $\alpha$ -Fe<sub>2</sub>O<sub>3</sub> hybrid nanocomposites. *Synth. Met.* **2015**, *204*, 1–9. [\[CrossRef\]](#)
18. Zhao, T.; Ren, Y.; Jia, G.Y.; Zhao, Y.; Fan, Y.; Yang, J.; Zhang, X.; Jiang, W.; Wang, L.; Wei, L. Facile synthesis of mesoporous WO<sub>3</sub>@graphene aerogel nanocomposites for low-temperature acetone sensing. *Chin. Chem. Lett.* **2019**, *30*, 2032–2038. [\[CrossRef\]](#)
19. Abu Hussein, N.A.; Hawari, H.F.; Wong, Y.H. Synthesis of Iron Oxide/Polyaniline/Reduced Graphene Oxide Nanocomposite Materials as Active Sensing Material. In Proceedings of the 2020 8th International Conference on Intelligent and Advanced Systems (ICIAS), Kuching, Malaysia, 13–15 July 2021. [\[CrossRef\]](#)
20. Dong, Z.M.; Xia, Q.; Ren, H.; Shang, X.; Lu, X.; Joo, S.W.; Huang, J. Preparation of hollow SnO<sub>2</sub>/ZnO cubes for the high-performance detection of VOCs. *Ceram. Int.* **2023**, *49*, 4650–4658. [\[CrossRef\]](#)
21. Foronda, J.R.F.; Aryaswara, L.G.; Santos, G.N.C.; Raghu, S.N.V.; Muflikhun, M.A. Broad-class volatile organic compounds (VOCs) detection via polyaniline/zinc oxide (PANI/ZnO) composite materials as gas sensor application. *Heliyon* **2023**, *9*, e13544. [\[CrossRef\]](#) [\[PubMed\]](#)
22. Zhao, H.; Zhang, T.; Qi, R.; Dai, J.; Liu, S.; Fei, T.; Lu, G. Development of solution processible organic-inorganic hybrid materials with core-shell framework for humidity monitoring. *Sens. Actuators B Chem.* **2018**, *255*, 2878–2885. [\[CrossRef\]](#)
23. Liu, Z.; Yang, X.; Huo, L.; Tian, X.; Qi, T.; Yang, F.; Wang, X.; Yu, K.; Ma, F.; Sun, J. P-CuPcTS/n-SnO<sub>2</sub> organic-inorganic hybrid film for ppb-level NO<sub>2</sub> gas sensing at low operating temperature. *Sens. Actuators B Chem.* **2017**, *248*, 324–331. [\[CrossRef\]](#)
24. Kim, M.Y.; Hwang, J.Y.; Mirzaei, A.; Choi, S.-W.; Kim, S.-I.; Kim, H.-S.; Kim, S.-J.; Roh, J.W.; Choi, M.S.; Lee, K.H.; et al. NO<sub>2</sub> Gas Sensing Properties of Ag-Functionalized Porous ZnO Sheets. *Adsorpt. Sci. Technol.* **2023**, *2023*, 9021169. [\[CrossRef\]](#)
25. Andre, R.S.; Mercante, L.A.; Facure, M.H.M.; Mattoso, L.H.C.; Correa, D.S. Enhanced and selective ammonia detection using In<sub>2</sub>O<sub>3</sub>/reduced graphene oxide hybrid nanofibers. *Appl. Surf. Sci.* **2019**, *473*, 133–140. [\[CrossRef\]](#)
26. Zhang, B.; Cheng, M.; Liu, G.; Gao, Y.; Zhao, L.; Li, S.; Wang, Y.; Liu, F.; Liang, X.; Zhang, T.; et al. Room temperature NO<sub>2</sub> gas sensor based on porous Co<sub>3</sub>O<sub>4</sub> slices/reduced graphene oxide hybrid. *Sens. Actuators B Chem.* **2018**, *263*, 387–399. [\[CrossRef\]](#)

27. Lee, Z.Y.; Hawari, H.F.B.; Djaswadi, G.W.; Kamarudin, K. A Highly Sensitive Room Temperature CO<sub>2</sub> Gas Sensor Based on SnO<sub>2</sub>-rGO Hybrid Composite. *Materials* **2020**, *14*, 522. [[CrossRef](#)]
28. Drmosh, Q.A.; Yamani, Z.H.; Hendi, A.H.; Gondal, M.A.; Moqbel, R.A.; Saleh, T.A.; Khan, M.Y. A novel approach to fabricating a ternary rGO/ZnO/Pt system for high-performance hydrogen sensor at low operating temperatures. *Appl. Surf. Sci.* **2019**, *464*, 616–626. [[CrossRef](#)]
29. Hussain, N.H.I.; Mustafa, M.K.; Asman, S. Synthesis of PANI/Iron (II, III) Oxide Hybrid Nanocomposites Using SolGel Method. *J. Sci. Technol.* **2018**, *10*, 1–4. [[CrossRef](#)]
30. Li, Y.; Zhao, H.; Ban, H.; Yang, M. Composites of Fe<sub>2</sub>O<sub>3</sub> nanosheets with polyaniline: Preparation, gas sensing properties and sensing mechanism. *Sens. Actuators B Chem.* **2017**, *245*, 34–43. [[CrossRef](#)]
31. Abokifa, A.A.; Haddad, K.; Fortner, J.; Lo, C.S.; Biswas, P. Sensing mechanism of ethanol and acetone at room temperature by SnO<sub>2</sub> nano-columns synthesized by aerosol routes: Theoretical calculations compared to experimental results. *J. Mater. Chem. A* **2018**, *6*, 2053–2066. [[CrossRef](#)]
32. Sydulu Singu, B.; Srinivasan, P.; Pabba, S. Benzoyl Peroxide Oxidation Route to Nano Form Polyaniline Salt Containing Dual Dopants for Pseudocapacitor. *J. Electrochem. Soc.* **2011**, *159*, A6–A13. [[CrossRef](#)]
33. Amir Faiz, M.S.; Che Azurahaman, C.A.; Raba'ah, S.A.; Ruzniza, M.Z. Low cost and green approach in the reduction of graphene oxide (GO) using palm oil leaves extract for potential in industrial applications. *Results Phys.* **2020**, *16*, 102954. [[CrossRef](#)]
34. Manna, R.; Srivastava, S.K. Reduced Graphene Oxide/Fe<sub>3</sub>O<sub>4</sub>/Polyaniline Ternary Composites as a Superior Microwave Absorber in the Shielding of Electromagnetic Pollution. *ACS Omega* **2021**, *6*, 9164–9175. [[CrossRef](#)] [[PubMed](#)]
35. Mathew, J.; Sathishkumar, M.; Kothurkar, N.K.; Senthilkumar, R.; Sabarish Narayanan, B. Polyaniline/Fe<sub>3</sub>O<sub>4</sub>-RGO Nanocomposites for Microwave Absorption. *IOP Conf. Ser. Mater. Sci. Eng.* **2018**, *310*, 012138. [[CrossRef](#)]
36. Kumar, R.; Youssry, S.M.; Ya, K.Z.; Tan, W.K.; Kawamura, G.; Matsuda, A. Microwave-assisted synthesis of Mn<sub>3</sub>O<sub>4</sub>-Fe<sub>2</sub>O<sub>3</sub>/Fe<sub>3</sub>O<sub>4</sub>@rGO ternary hybrids and electrochemical performance for supercapacitor electrode. *Diam. Relat. Mater.* **2020**, *101*, 107622. [[CrossRef](#)]
37. Patil, V.S.; Thoravat, S.S.; Kundale, S.S.; Dongale, T.D.; Patil, P.S.; Jadhav, S.A. Synthesis and testing of polyaniline grafted functional magnetite (Fe<sub>3</sub>O<sub>4</sub>) nanoparticles and rGO based nanocomposites for supercapacitor application. *Chem. Phys. Lett.* **2023**, *814*, 140334. [[CrossRef](#)]
38. Cai, H.; Feng, C.; Xiao, H.; Cheng, B. Synthesis of Fe<sub>3</sub>O<sub>4</sub>/rGO@PANI with three-dimensional flower-like nanostructure and microwave absorption properties. *J. Alloys Compd.* **2022**, *893*, 162227. [[CrossRef](#)]
39. Mondal, S.; Rana, U.; Malik, S. Reduced Graphene Oxide/Fe<sub>3</sub>O<sub>4</sub>/Polyaniline Nanostructures as Electrode Materials for an All-Solid-State Hybrid Supercapacitor. *J. Phys. Chem. C* **2017**, *121*, 7573–7583. [[CrossRef](#)]
40. Ahirrao, D.J.; Pal, A.J.; Singh, V.; Jha, N. Nanostructured porous polyaniline (PANI) coated carbon cloth (CC) as electrodes for flexible supercapacitor device. *J. Mater. Sci. Technol.* **2021**, *88*, 168–182. [[CrossRef](#)]
41. Ma, Y.; Zhou, Y.; Sun, Y.; Chen, H.; Xiong, Z.; Li, X.; Shen, L.; Liu, Y. Tunable magnetic properties of Fe<sub>3</sub>O<sub>4</sub>/rGO/PANI nanocomposites for enhancing microwave absorption performance. *J. Alloys Compd.* **2019**, *796*, 120–130. [[CrossRef](#)]
42. Gupta, M.; Hawari, H.F.; Kumar, P.; Burhanudin, Z.A. Copper Oxide/Functionalized Graphene Hybrid Nanostructures for Room Temperature Gas Sensing Applications. *Crystals* **2022**, *12*, 264. [[CrossRef](#)]
43. Zhang, D.Z.; Wu, Z.L.; Zong, X.Q. Metal-organic frameworks-derived zinc oxide nanopolyhedra\_S, N\_ graphene quantum dots\_polyaniline ternary nanohybrid for high-performance acetone sensing. *Sens. Actuators B Chem.* **2019**, *288*, 232–242. [[CrossRef](#)]
44. Gupta, M.; Abu Hussein, N.A.; Fahmi Hawari, H. Graphene derivative coated QCM-based gas sensor for volatile organic compound (VOC) detection at room temperature. *Indones. J. Electr. Eng. Comput. Sci.* **2020**, *18*, 1279–1286. [[CrossRef](#)]
45. Jiang, T.; Wang, Z.; Li, Z.; Wang, W.; Xu, X.; Liu, X.; Wang, J.; Wang, C. Synergic effect within n-type inorganic-p-type organic nano-hybrids in gas sensors. *J. Mater. Chem. C* **2013**, *1*, 3017–3025. [[CrossRef](#)]
46. Yan, Y.; Yang, G.; Xu, J.L.; Zhang, M.; Kuo, C.C.; Wang, S.D. Conducting polymer-inorganic nanocomposite-based gas sensors: A review. *Sci. Technol. Adv. Mater.* **2021**, *21*, 768–786. [[CrossRef](#)]
47. Abu Hussein, N.A.; Hawari, H.F.; Wong, Y.H.; Haseeb, A.S.M.A. Preparation and sensing characterization of hybrid iron oxide/polyaniline/reduced graphene oxide at room temperature. *Int. J. Chem. Biochem. Sci.* **2021**, *20*, 90–95.
48. Shafa, M.; Priante, D.; ElAfandy, R.T.; Hedhili, M.N.; Mahmoud, S.T.; Ng, T.K.; Ooi, B.S.; Najar, A. Twofold Porosity and Surface Functionalization Effect on Pt-Porous GaN for High-Performance H<sub>2</sub>-Gas Sensors at Room Temperature. *ACS Omega* **2019**, *4*, 1678–1684. [[CrossRef](#)]
49. Nabeel, M.; Varga, M.; Kuzsella, L.; Fiser, B.; Vanyorek, L.; Viskolcz, B. The Effect of Pore Volume on the Behavior of Polyurethane-Foam-Based Pressure Sensors. *Polymers* **2022**, *14*, 3652. [[CrossRef](#)]

**Disclaimer/Publisher's Note:** The statements, opinions and data contained in all publications are solely those of the individual author(s) and contributor(s) and not of MDPI and/or the editor(s). MDPI and/or the editor(s) disclaim responsibility for any injury to people or property resulting from any ideas, methods, instructions or products referred to in the content.